Lead-DBS: A toolbox for deep brain stimulation electrode localizations and visualizations

Andreas Horn [a,b,*], Andrea A. Kühn [a]

[a] Department of Neurology, Movement Disorders Unit, Charité — University Medicine (CVK), Berlin, Germany
[b] Center for Adaptive Rationality (ARC), Max-Planck-Institute for Human Development, Berlin, Germany

ARTICLE INFO

ABSTRACT

To determine placement of electrodes after deep brain stimulation (DBS) surgery, a novel toolbox that facilitates both reconstruction of the lead electrode trajectory and the contact placement is introduced. Using the toolbox, electrode placement can be reconstructed and visualized based on the electrode-induced artifacts on post-operative magnetic resonance (MR) or computed tomography (CT) images.

Correct electrode placement is essential for efficacious treatment with DBS. Post-operative knowledge about the placement of DBS electrode contacts and trajectories is a promising tool for clinical evaluation of DBS effects and adverse effects. It may help clinicians in identifying the best stimulation contacts based on anatomical target areas and may even shorten test stimulation protocols in the future.

Fifty patients that underwent DBS surgery were analyzed in this study. After normalizing the post-operative MR/CT volumes into standard Montreal Neurological Institute (MNI)-stereotactic space, electrode leads (n = 104) were detected by a novel algorithm that iteratively thresholds each axial slice and isolates the centroids of the electrode artifacts within the MR/CT-images (MR only n = 32, CT only n = 10, MR and CT n = 8). Two patients received four, the others received two quadripolar DBS leads bilaterally, summing up to a total of 120 lead localizations. In a second reconstruction step, electrode contacts along the lead trajectories were reconstructed by using templates of electrode tips that had been manually created beforehand. Reconstructions that were made by the algorithm were finally compared to manual surveys of contact localizations.

The algorithm was able to robustly accomplish lead reconstructions in an automated manner in 98% of electrodes and contact reconstructions in 69% of electrodes. Using additional subsequent manual refinement of the reconstructed contact positions, 118 of 120 electrode lead and contact reconstructions could be localized using the toolbox.

Taken together, the toolbox presented here allows for a precise and fast reconstruction of DBS contacts by proposing a semi-automated procedure. Reconstruction results can be directly exported to two- and three-dimensional views that show the relationship between DBS contacts and anatomical target regions. The toolbox is made available to the public in form of an open-source MATLAB repository.

© 2014 Elsevier Inc. All rights reserved.

Introduction

Deep brain stimulation surgery (DBS) is a highly efficacious treatment option for patients with severe movement disorders such as Parkinson's disease (PD), dystonia and essential tremor (ET). Improvement in motor symptoms as well as quality of life have been proven in several multicenter studies for PD (Deuschl et al., 2006; Krack et al., 2003; Schupbach, 2005); for dystonia (Kupsch et al., 2006; Mueller et al., 2008; Vidailhet et al., 2005; Volkmann et al., 2012); and for ET (Hariz et al., 2008; Schuurman et al., 2000).

Additionally to the DBS stimulation parameters, the correct anatomical description of the electrode contact placements determines the area that is being stimulated and has a major influence on the clinical outcome of chronic DBS. Studies in PD patients undergoing STN DBS have shown that accuracy of electrode placement within the anatomical target region correlates with the motor improvement during DBS (for example Frankemolle et al., 2010; Welter et al., 2014; Wodarg et al., 2012). Similarly, the degree of motor improvement with DBS in dystonia was related to electrode position within the pallidum (Schönecker et al., 2014; Tisch et al., 2007). Although other factors influence the clinical outcome of DBS (Lumsden et al., 2013; Vidailhet et al., 2005), contact mislocation is considered to be the most common cause of a poor clinical response (Ellis et al., 2008; Marks et al., 2009). Accordingly, knowledge about localizations of contacts can be supportive in clinical routines to evaluate DBS effects and may help to define the

* Corresponding author at: Department for Neurology, Movement Disorders Unit, Charité — University Medicine (CVK), Augustenburger Platz 1, 13353 Berlin, Germany.
E-mail address: andreas.horn@charite.de (A. Horn).

best contact for chronic DBS, especially in more complex electrode designs with multiple contacts that will be available in the near future.

Moreover, information on electrode localization is crucial for various scientific approaches using depth recordings from DBS target regions of the basal ganglia (Brown and Williams, 2005) or stimulation protocols to evaluate the involvement of the anatomical DBS target region in information processing (Cavanagh et al., 2011; Frank et al., 2007; Green et al., 2013).

Evaluation of electrode placement can be achieved by postoperative magnetic resonance (MR)- or computer tomography (CT)- imaging. Depending on the DBS center, usually one imaging method is established in clinical routines. Electrode placement is most often denoted relative to the anterior commissure–posterior commissure (AC–PC) stereotactic space (in a systematic review, electrode coordinates in this notation were found in 8 of 13 studies; Caire et al., 2013) or within the standardized MNI space (e.g. see Schönecker et al., 2009; Witt et al., 2013). The former method requires manual measurements that are prone to significant inaccuracies (Pallavaram et al., 2008) and does not take anatomical inter-subject variability into account (Starr et al., 1999; Zhu et al., 2002). On the other hand, warping subject-specific anatomic images into a well-defined standard space as the MNI space makes electrode placements comparable over subjects and DBS centers. This also makes it possible to set electrode contacts into relationship with atlas data of target regions (for examples of available subcortical atlas data, e.g. see Jakab et al., 2012; Keuken et al., 2013, 2014; Prodoehl et al., 2008; Sarnthein et al., 2013; Tzourio-Mazoyer et al., 2002; Yelnik et al., 2003).

After the normalization of MR-images, a time-consuming and observer-dependent manual survey of electrode contacts has usually to take place to determine their positions. This can be done by manually analyzing the terminal portion of the quadripolar DBS electrodes composed of four metallic (platinium/iridium) non-insulated contacts at equidistant intervals which generate susceptibility artifacts on the postoperative MR image (Schönecker et al., 2009). The centers of the artifacts show hypo-intense and represent the centers of the electrode contacts (Pollo et al., 2004; Yelnik et al., 2003; Fig. 1). Usually, this is performed by using a slice-based (two-dimensional, 2D) MR-viewing software, and fiducial landmarks are manually placed upon the electrode contact artifacts.

To overcome the necessity of a manual survey of electrode contacts and to increase precision in this process, we introduce a toolbox to determine the electrode contact coordinates in a semi-automated design. The primary goal is to enable the user with a tool that provides a good starting-point for fast manual fine adjustment of DBS contact localization.

Methods

Patients and imaging

In total, fifty patients (33 male; mean age 44.5 ± 17.45 yrs [mean ± SD], range 13–75 yrs) that underwent DBS surgery were analyzed in this study. Two patients received four, the others received two quadripolar DBS leads bilaterally (Medtronic, Minneapolis, Minnesota, US). To include different electrode target regions, clinical indications and electrode models, patients were randomly selected from a large database of DBS patients treated at our center (~550 patients). Forty patients received postoperative MR-imaging, eight of whom also underwent post-operative CT imaging. Ten other patients were evaluated solely by CT-imaging postoperatively (summing up to a total of eighteen patients with CT-imaging). Twenty-four PD patients were included that had undergone electrode implantation targeting at the STN, twenty patients with idiopathic dystonia had undergone stereotactic surgery with electrode target placement in the internal part of the globus pallidus internus (GPi). Two of these received additional electrodes in the ventromedial internal nucleus (ViM) of the thalamus for dystonic tremor as did six patients affected by ET. Thirty-three patients received Medtronic DBS leads of model 3389 (contact-to-contact distance of 0.5 mm, 2 mm distance between centers of two adjacent contacts) and seventeen patients received DBS leads of model 3387 (contact-to-contact distance of 1.5 mm with 3 mm distance between centers of adjacent contacts). Table 1 summarizes patient demographics and clinical indications.

All patients underwent pre-operative MR-imaging on a 1.5 T scanner (NT Intera; Philips Medical Systems, Best, The Netherlands) using a T2-weighted fast spin-echo (FSE) with the following parameters: TR = 3500 ms, TE = 138 ms, echo-train length: 8, excitations: 3, flip angle: 90°, section thickness: 2 mm, section gap: 0.2 mm, FOV: 260 mm (in-plane resolution 0.51 × 0.51 mm), matrix size: 384 interpolated to 512, total acquisition time, 10 min and 41 s.

Postoperative MR-imaging was performed in 40 patients. DBS patients are subject to a limitation of the specific absorption rate (SAR, <0.1 W/kg), which has been specified by the manufacturer of the electrodes. Within 5 days after implantation of the electrodes, MR-imaging was performed on the same scanner using a T2-weighted fast spin-echo (FSE) sequence in low SAR mode with the same parameters as used pre-operatively. Philips software Version 11.1 level 4 was used. MR sections in the axial and coronal planes were obtained and processed in this study. In the following, "axial" and "coronal" volumes refer to acquisitions with voxel sizes of 0.51 × 0.51 mm in the axial or coronal planes respectively, each with a 2 mm slice thickness.
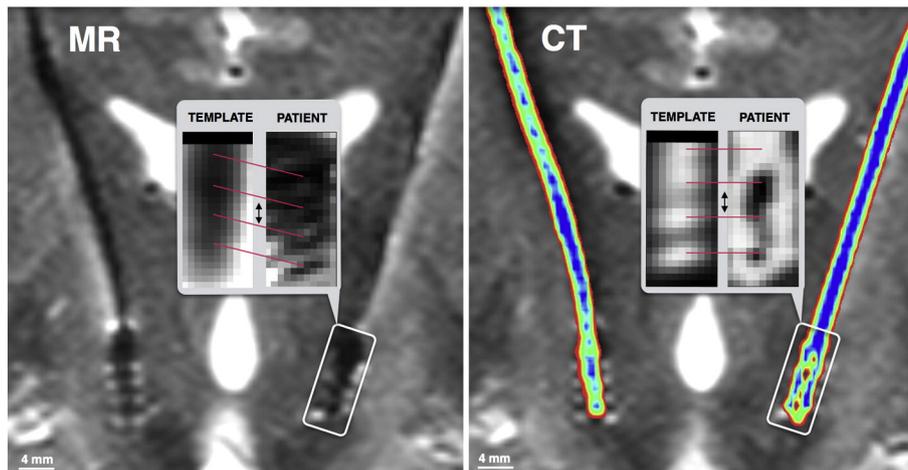

Fig. 1. Coronal slice showing the artifacts induced by the deep brain stimulation electrodes. MR (left) superimposed with CT (right) imaging results of the same patient are shown here. In the middle of both images, the template of the electrode tip for MR and CT electrodes are depicted next to the tip of the actual patient. "CORE" cross-correlates the two volumes to find the best match. In this example, the template of the MR-volume must be moved slightly down to find the best match, whereas the CT template is shown in good alignment with the electrode tip of the patient. A Medtronic 3389 electrode model was used on this patient.

Table 1
Patient demographics and target regions of DBS surgery.

Target region	Diagnosis	Total: # patients: 50 # electrodes: 104 (2 pts. received 4 electrodes)	Patients with postoperative MR/MR + CT/CT
Subthalamic nucleus (STN)	Parkinson's disease	# 24 pts., 48 electrodes	14/8/2
Internal globus pallidum (GPi)	Dystonia	# 18 pts., 36 electrodes	13/0/5
Ventromedial internal nucleus of the thalamus (VIM)	Essential tremor	# 6 pts., 12 electrodes	5/0/1
Both GPi and VIM	Dystonic tremor	# 2 pts., 8 electrodes	0/0/2
Gender	# 33 male	# 17 female	
Age	ø 44.5, ± SD 17.4 years		

Postoperative CT was conducted in 18 patients (8 of whom also had postoperative MRI). Here, high-resolution images were acquired on a LightSpeed16 (GE Medical System, Milwaukee, Wisconsin) Slice CT with a spatial resolution of $0.49 \times 0.49 \times 0.67$ mm³. Images were acquired in axial (i.e. sequential/incremental) order at 140 kV and automated mA setting. Noise index was 7.0. A large SFOV with 50 cm diameter was used.

Preprocessing of MR-images

Normalization of MR-images was performed following the approach of Schönecker et al., using FSL 5 (http://fsl.fmrib.ox.ac.uk/fsl/fslwiki/) and the ICBM 152 Nonlinear 2009b template (Fonov et al., 2011). This included a three-step linear normalization routine, where each of the steps was weighted by a smaller mask. Thus, each step increasingly focused on the subcortical area of interest. In more detail, after a co-registration step between the "coronal" and "axial" volumes, a global linear normalization of axial images was performed, followed by one that focused on a large subcortical volume. In the last step, axial images were further normalized by using a mask that merely included a volume around the subcortical target structures and spared the ventricles. As none of the three normalization steps used nonlinear deformation fields, electrode contacts remained equidistant on a straight line in the normalized volumes and artifacts still displayed a similar shape as in the non-normalized raw data acquired by the scanner. This linear normalization algorithm is able to normalize volumes with high accuracy (resulting in a spatial dispersion towards predefined reference points of a root mean square difference error of 1.29 ± 0.78 mm). The resulting subcortical volumes exhibited cubic bounding boxes (e.g. definable by two points in MNI-space at $-55, 45, 9.5$ and $55, -65, -25.0$ mm) of interpolated volumes in high resolution (voxel sizes: $0.216 \times 0.216 \times 0.216$ mm) from both the axial and coronal MR acquisitions. Each of the two volumes showed exactly the same orientation and number of voxels; thus, combined versions of both volumes could be generated, e.g. by voxel-wise averaging or multiplying. When "default parameters" (see below) were applied, for the first algorithm ("TRAC") the two images were averaged and smoothed by a Gaussian kernel $3 \times 3 \times 3$ mm in size.

Preprocessing of CT-images

Postoperative CT images were coregistered to preoperative MR images using 3DSlicer 4 (http://www.slicer.org/). Images were then normalized into MNI space with the same algorithm as described in the previous section which used the pre-operative MR images for estimation and applied the final normalization parameters to the CT images. This process resulted in a single normalized CT volume in high resolution (voxel size: $0.216 \times 0.216 \times 0.216$ mm, bounding box: $-55, 45, 9.5$ and $55, -65, -25.0$ mm).

Semiautomated reconstruction

The process can be divided into two steps. First, the anatomical course of the lead trajectory is reconstructed, resulting in a straight line that traverses through the three-dimensional (3D) volume of the brain. Please note that the reconstruction of the lead itself may not accurately model its long-term placement due to brain-shift and postoperative bending of the electrodes (Kim et al., 2010; van den Munckhof et al., 2010), but is a necessary processing step to reconstruct contact positions. As a second step, placement of the four electrode contacts that are represented as a shape of a pearl-string/bailey-bead-formation on the MR-images can be determined at the end of this line.

Reconstruction of the electrode lead trajectory ("TRAC")

The following algorithm could be used for DBS electrode reconstructions based on both MR and CT images. However, image intensities of CT images were multiplied by -1. This results in low-intensity values for the trajectory of the DBS lead region in both imaging modalities.

The algorithm started on the dorsal-most axial slice of the axial MR or the CT volumes (in MNI-space, this corresponds to a z-height of 9.5 mm). Using a quite large mask (bounded by MNI-coordinates: $+/- 7.2$ 12.9 9.5 and $+/-39.6$–19.5 9.5 for the two sides, respectively) that covered all trajectories at this height, the trajectory was identified by thresholding the intensity values of the axial plane within the mask. A suitable threshold was determined by adding $a = 0.9 \times$ standard-deviations to the mean of all intensity values within the mask. As a result one cluster (most often of oval shape) usually defined the electrode artifact. Value a was further adjusted by the algorithm if all intensity-values were lower than the resulting threshold. The centroid of the isolated cluster was used as a starting point of the electrode trajectory.

The second slice could be analyzed by already using a much smaller mask, by default 20×20 pixels in size, that was placed around the location of the cluster found on the first slice. From the third slice on, the small mask was moved to surround the coordinates of where the next point was expected, based on the two or more cluster-centroid coordinates that had been isolated on prior slices. Thus, the algorithm worked its way through the subcortical volume in dorsoventral direction, until a trajectory artifact could no longer be detected or until a z-coordinate below -15.5 mm was reached; based on our experience, no electrode artifact should be visible here anymore (regardless whether the anatomical target region is STN, GPi or ViM). If more than two clusters were isolated by thresholding the area within the mask, the algorithm decided for the one closer to where the next trajectory point was expected based on prior information. This first algorithm described here was dubbed "TRAC" (**tra**jectory se**c**arch) for brevity reasons and is summarized in pseudocode in box "Algorithm 1" (also see Fig. 2).

Algorithm 1. "TRAC": trajectory reconstruction

```
Input   Start with dorsal-most axial slice S(1) of axial MR-volume.
Output  Fitted line of trajectory reconstruction L
1:      Isolate region on S(1) using large heuristical mask
2:      Threshold region isolated by the mask to determine centroid C(1)
3:      Isolate region on S(2) using small mask around coordinates of C(1)
4:      Threshold region isolated by the mask to determine centroid C(2)
5:      Compute line L between C(1) and C(2)
6:      for i=3:last_slice do
7:          compute point E where next centroid is expected based on L
8:          Isolate region R from S(i) using small mask centered at E
9:          Threshold R to determine centroid C(i)
10:         if more than 2 clusters found then
11:             decide for cluster with centroid closer to E end if
12:         if C(i) can't be defined then break for loop end if
13:         if i represents slice below z=-15.5 then break for loop end if
14:         Fit line L to data points C(1:i)
15:     end for
```

Based on a large number (n = 374) of electrode trajectories that had been reconstructed in our center, standard traversing directions of left and right electrodes could be empirically defined by normalizing the traversing direction vector to a distance of 1. Based on this data, the algorithm marked trajectory reconstructions as questionable if their traversing direction was more than four standard-deviations off the mean trajectory course (see Fig. S1). This functionality helps to automatically classify doubtful reconstructions, which can then be further examined manually.

Reconstruction of electrode contact positions ("CORE")

In both MR- and CT-modalities, the electrode contacts can be easily moved along the trajectory in a manual correction step, which in practice renders the success of "CORE" following below less important than "TRAC" described above. To localize electrode contacts along the reconstructed trajectory, in a first step, templates of the most ventral part of the lead trajectory were prepared by manually cutting out the region around the tip of the electrode in 5 patients for the Medtronic 3389 and 3387 electrodes for CT and MR images respectively. For each electrode, a cubic region of $11 \times 11 \times 23$ (Medtronic 3389) or $11 \times 11 \times 30$ (3387) voxels ($2.4 \times 2.4 \times 11.5/15$ mm) was cut out orthogonally to each trajectory (in such a way that it traversed vertically through the volume, exactly through its center, see Figs. 1 and 2C). This resulted in 10 cuboid volumes that were averaged to build two templates of the electrode tip for each imaging modality.

In a second step, to reconstruct the electrode heights alongside the trajectory, the algorithm similarly sampled a cubic volume of $11 \times 11 \times n$ voxels orthogonally to the trajectory course. Here, n was the length of the reconstructed trajectory in voxels. This resulted in a cuboid volume through which the electrode trajectory traversed vertically and exactly in its middle. To determine electrode contact heights along the lead trajectory, each $1 \times 1 \times n$ column of the volume was then cross-correlated with the according $1 \times 1 \times 23/30$ column of the template volume. Cross-correlation sequences of all columns were averaged and the peak of the averaged sequence was used to determine the offset of the template to the empirical data, i.e. the height of electrode contacts.

In analogy to the first algorithm, this second one received the acronym "CORE" for "**co**ntact **re**construction" and is summarized in pseudocode (see box "Algorithm 2" and Fig. 2).

Algorithm 2. "CORE": reconstruction of electrode contact positions

```
Input    3 × n coordinates describing fitted line of trajectory reconstruction L,
         Coronal cubic MR-volume VCor and 11 × 11 × 30 voxels template of electrode
         artifacts T
Output   Coordinates of four electrode contacts EC
1:       Sample volume VS n × 11 × 11 voxels orthogonally around L
2:       for z=0:n-30 do
3:           for x=1:11 do
4:               for y=1:11 do
5:                   create Pearson's correlation coefficient z:z+30 × x × y vector of
                     VS with 1:30 × x × y vector of T, store as Corr(x,y,z)
6:               end for
7:           end for
8:       end for
9:       average Corr over first two dimensions and find maximum of resulting 1 × n-30
         vector mCorr which denotes the height of optimal fit from
         final portion of the electrode artifact in VS to T
```

Comparison with manually localized electrode contacts

To evaluate the quality of fit of the automated reconstructions, both lead trajectories and electrode contacts were compared to a manual survey of electrode localizations. Reconstructions were classified as "correct" if the (perpendicular) Euclidean distances between manual contact and automated trajectory/contact reconstructions were smaller than 2 mm (as amounts to the approximate diameter of the trajectory artifacts).

Here, the aim of the automatic placement should be seen as an assisting method for fast and robust electrode localizations to facilitate its manual fine adjustment. Moreover, it is important to note that in our study we defined a "correct" electrode placement in relation to a previous determination of electrode placement by manual reconstruction in order to describe the validity of the reconstruction by the toolbox. However, without histological confirmation, DBS electrode reconstruction always remains presumptive.
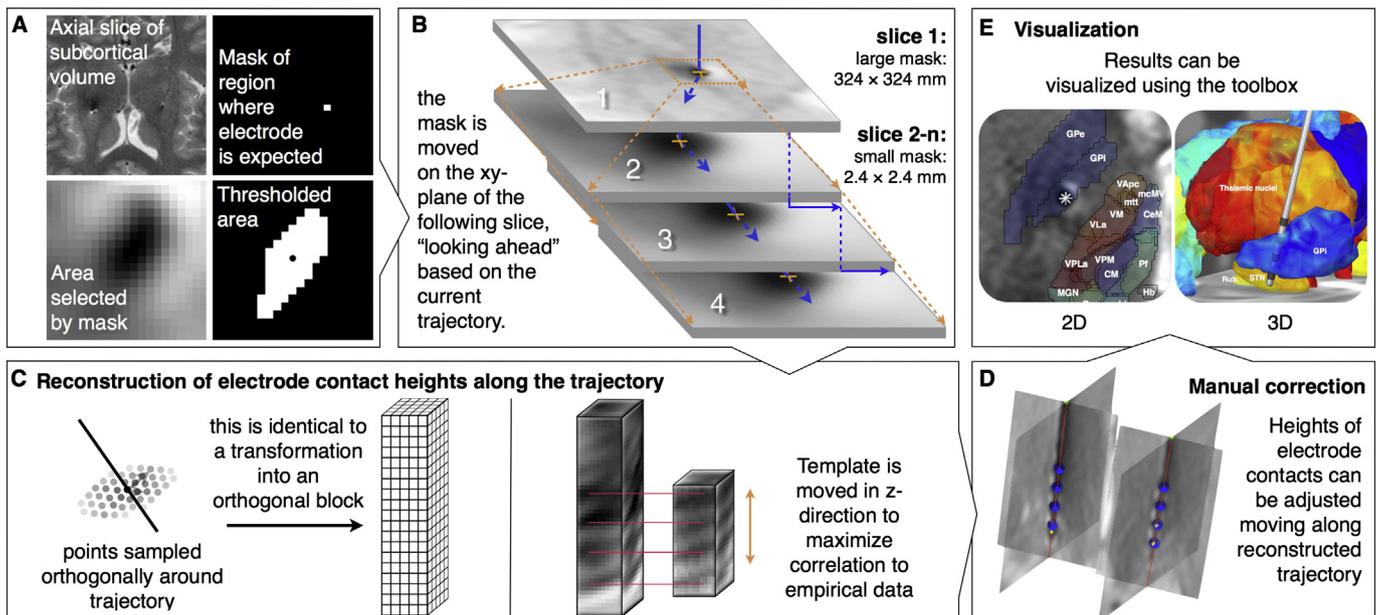

Fig. 2. Methodological steps of DBS-electrode reconstruction. A) An axial slice (upper left) is loaded into memory and masked either by a large heuristic mask (first slice) or by a small mask (further slices, see upper right) based on reconstructions in prior slices. The area selected by the mask (lower left) is thresholded (lower right) and the centroid of the thresholded area defines the new point in the trajectory. B) In this way, the trajectory course is estimated. The mask that selects an area of interest of each slice is moved to the x-y-coordinates, on which the new point in the trajectory is expected based on prior slices. C) Once the trajectory has been estimated, a cuboid volume is sampled alongside the reconstructed trajectory. To determine the heights of electrode contacts on the trajectory, a manually created template of the electrode tip is cross-correlated with this volume. D) The toolbox gives estimates of electrode contact positions alongside the trajectory at the height defined by a peak in the cross-correlation sequence. Two-dimensional planes are visualized orthogonally to the trajectory, allowing for an easy manual adjustment of electrode heights. E) Finally, results can be visualized in synopsis with anatomical atlas data.

Visualization of atlas data

To visualize atlas data in synopsis with the electrode reconstruction results, atlas data can be read in by the toolbox in standard nifti-file format (http://nifti.nimh.nih.gov/). The atlas data can be visualized in 2D-slice views as sliced overlays on the MR-images, or in 3D-reconstructions (Figs. 3–4). To compute the latter, xyz-coordinates of all non-zero voxels in the atlas volumes are read from the nifti-image, and their isovolume of a certain intensity is computed. In this study, binary atlas data was visualized, i.e. volumes had an intensity of one within the region and zero outside. Thus, the isovalue used for 3D-reconstructions was set to one.

Results

Reconstruction results

In MR imaging, using default parameters, 72 of 80 (90%) reconstructions found the correct trajectory. Fifty-five of 80 (69%) electrode contact heights were correctly reconstructed using default parameters. By slightly adjusting individual parameters in cases that yielded faulty reconstructions, a total of 78 (98%) trajectory reconstructions and 61 (76%) electrode contact heights were reconstructed correctly. Such parameter adjustments involved whether the images should be slightly smoothed or not, whether the axial and coronal versions of the images should be point-wise multiplied with each other or sharpened with an exponent of 10 (for a list of parameters, see Table 2). An additional crucial parameter that had to be changed in MR imaging in some cases was the size of the mask that cuts out a square region around the trajectory on the axial planes, since in some patients, electrode trajectories produced larger artifacts than in others, most likely due to local edema in the first days after implantation. All parameters that were changed to yield better results in individual cases can be easily set in several option-fields of the toolbox and only affect the most crucial success of "TRAC" (whereas "CORE" is not affected by changes of parameters).

In CT imaging, 40 leads were reconstructed (resulting from 16 patients with 2 leads and 2 patients with 4 leads). Due to the good contrast of the DBS-lead in CT imaging, "TRAC" was able to correctly find all 40 (100%) electrode reconstructions using default parameters. "CORE" could determine the correct height of electrode contacts along the lead-trajectory in 22 of 40 (55%) reconstructions, however, since reconstructions can be easily moved along the trajectory, this led to a 100% success rate in the overall semi-automatic reconstruction process.

In summary, the most important result was the final success rate of lead trajectory reconstructions (98% MR and 100% CT imaging), because i) parameters could be easily adjusted if "TRAC" failed and ii) once the lead trajectory reconstruction succeeded, the heights of electrode contacts could be manually moved alongside the trajectory using the toolbox (Fig. 2 D). Thus, when incorporating such manual correction steps, 98.3% of both electrode leads and contacts could be reconstructed using the toolbox, regardless of the imaging modality applied. Two (MR) reconstructions failed right at the start of the reconstruction task (where a large heuristic mask was used to isolate the artifact) because of an unusual artifact shape in one case and a blood vessel that was mistaken for the electrode artifact on the first slice in the other case. Setting the starting point of the lead trajectory reconstruction manually is an option to deal with such issues and has already been implemented in the toolbox. The algorithm was able to classify both of the two faulty reconstructions as doubtful (see Fig. S1 — here, more faulty reconstructions are marked that resulted from runs with default parameters), since they either traversed in a completely different direction than usual trajectories or even exited the subcortical volume at some point. Besides, faulty reconstructions are easy to detect manually, using the built-in control view (Fig. 2 D).

Congruency between MR- and CT-imaging

A subset of eight patients underwent both CT and MR imaging postoperatively. Thus, results from both imaging modalities that had been processed and analyzed separately from each other could be directly compared. For this analysis, the optimal manual localization was used,
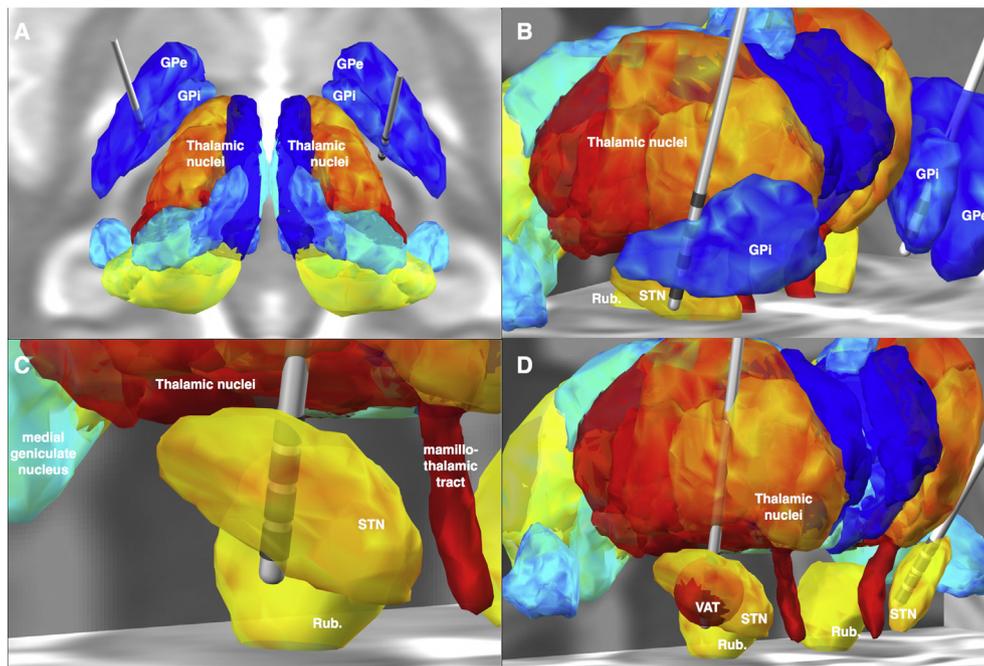

Fig. 3. Different views of the electrode scene viewer. Atlas data of subcortical nuclei are rendered in solid colors. For demonstrational purposes, two different atlas sets are combined in this compound figure. The morel atlas (Krauth et al., 2010) in a version that has been normalized to MNI space (Jakab et al., 2012), as well as the GPi/GPe volumes from the BGHAT atlas (Prodoehl et al., 2008) are shown. A) View from dorsal direction showing the different thalamic nuclei as well as biparted globus pallidus, B) Electrode trajectory in right GPi and C) right STN. D) Volume of activated tissue calculated following the approach of (Mädler and Coenen, 2012) for a monopolar voltage-steered stimulation of contact K1 at 3.5 V and an impedance of 1000 Ω in right STN.
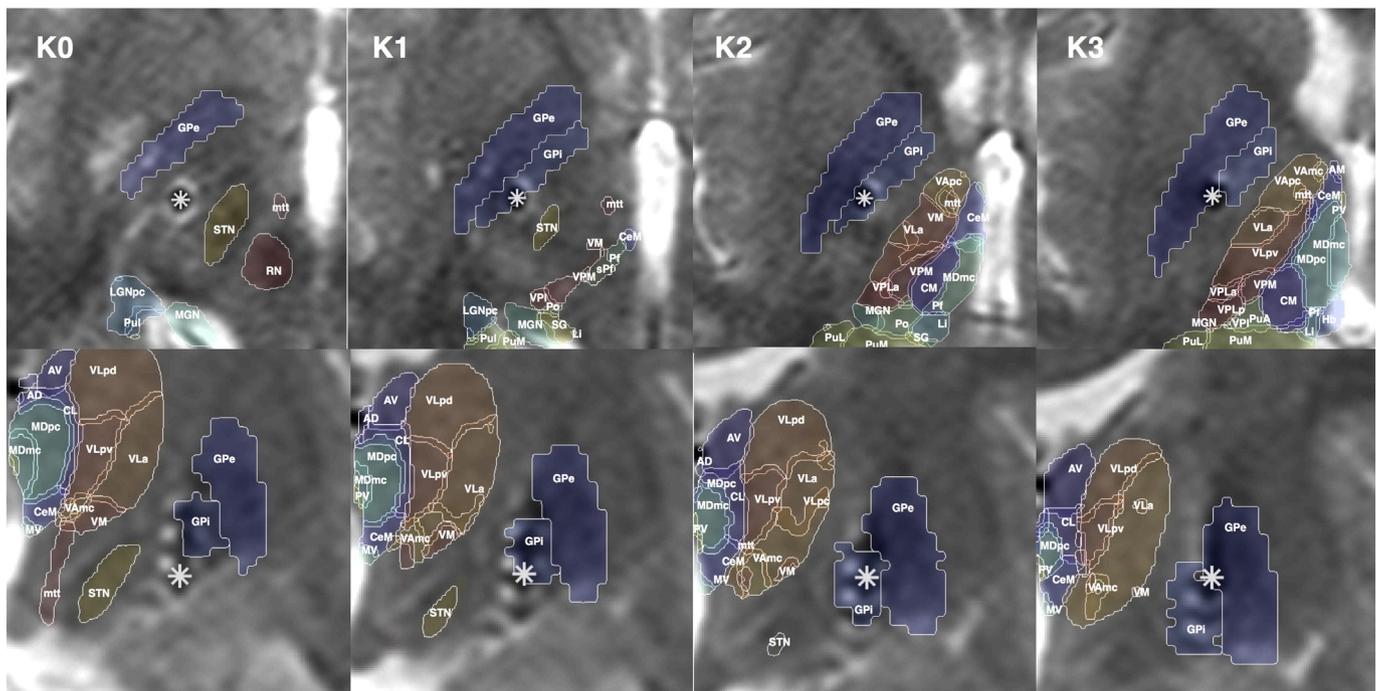
Fig. 4. Reconstruction of right electrode (target GPi) exported in axial (top) and coronal (bottom) slice views. GPi and GPe (blue) taken from (Prodoehl et al., 2008), STN (yellow), nucl. ruber (red) and thalamic nuclei (other colors) taken from (Jakab et al., 2012). K0 refers to the dorsalmost, K3 to the ventralmost right electrode contact. Abbreviations for thalamic nuclei are consistent with (Krauth et al., 2010) and can be found in Table S1.

i.e. in MR imaging, the automatic results were manually refined and in CT imaging, heights of electrodes were manually defined based on the trajectory found, both using the "manual correction" user interface of the toolbox. MNI-coordinates of localized electrodes highly correlated (Fig. S2) and had a mean mismatch of 0.66 mm (standard-deviation ± 0.43) throughout all 64 MR–CT contact pairs. This error is quite small given the fact that CT images were linearly co-registered to their corresponding preoperative MR images on a full-brain level and that the image resolution of both modalities is of comparable magnitude.

Discussion

In this study, we introduce an automated DBS electrode reconstruction algorithm. Analysis of a large group of patients (n = 50) showed that the algorithm can facilitate and improve the process of electrode and trajectory localization based on post-operative MR- or CT-images.

Auto-manual vs. purely manual reconstructions

By comparing a combination of automated and manual to purely manual reconstructions in this study, certain differences in their quality became evident. Most important to note is that purely manual electrode placement surveys are usually performed in a 2D slice viewer software. The hypointense/hyperdense electrode contact artifact can be visualized in a slice-viewer and defined by a point fiducial at its center

(Brücke et al., 2012; Pollo et al., 2004; Yelnik et al., 2003). This procedure does not ensure, however, that each electrode contact is situated i) within the correct distance to the next contact and ii) on a straight line with all other contacts. To address this issue, the algorithm proposed here obligatorily models the lead trajectory as a straight line and places the electrode contacts in equal distances to each other. Since the transformation (Schönecker et al., 2009) that is used to warp the individual MR-images into MNI space is a linear one (i.e. a 4×4 affine transformation matrix), and distances of contacts in MR-volumes correspond to their actual distances (Yelnik et al., 2003), the distances of electrode contacts can be accurately calculated even after normalization into MNI space. This method reduces the degrees of freedom in the reconstruction process of each single contact and thus makes the process more robust. When automatic localizations are manually refined by using the toolbox presented here, this advantage still holds, since contact localizations can only be moved along the trajectory as a group of four. If instead the trajectory itself is manually moved, all four contacts are moved as well. Thus, even if the automatic reconstructions are not always the best solution to the reconstruction problem, it is a great help if the automatic reconstructions are already close, making a manual refinement very fast and straight-forward. Using the toolbox, the lead trajectory can be manually moved with mouse or arrow keys in cases where the reconstruction is slightly off the artifact. Using the keyboard, electrode contact reconstructions can then be manually moved to their correct position along the trajectory line.

Table 2
List of important parameters used by "TRAC" (Algorithm 1).

Parameter name	Default	Comment
MR-data used	Mean image of axial and coronal MR-series	In some cases, usage of only the axial or coronal image yields superior results.
Smoothing of MR-data	Gaussian kernel of FWHM $3 \times 3 \times 3$ voxels	In some cases, smoothing may improve results.
Size of mask	21×21 voxels	The size of mask can be a critical parameter in "TRAC", especially when large artifacts are involved, e.g. due to local edema after electrode placement. Usage of smaller and larger masks can substantially change results.

Reconstructions in MNI- vs. native space

The algorithm proposed here works on normalized versions of single-subject MR/CT data, i.e. the brain volumes have to be co-registered to an MNI template before the algorithm can reconstruct the trajectory and electrode contacts. This is a crucial point, since advantages and disadvantages of processing in standard as opposed to native (i.e. unnormalized) space should be considered.

Disadvantages of reconstruction within the normalized space may lie in a slight loss of accuracy, since in the normalization step single subject proportions of brain anatomy may become skewed. This may result in small inaccuracies of the relationship between electrode contacts and target regions. In this context, it is important to note that the normalization routine applied here is a purely linear one (Schönecker et al., 2009), thus proportions are not modified in a nonlinear way (which might result in single electrode contacts becoming larger/smaller or the lead developing a distorted trajectory). Besides, the last of the three normalization steps uses a weighting mask that merely covers important regions like the basal ganglia and spares the ventricles (which may largely differ in magnitude, especially in elderly patients; Wu et al., 2009). However, the accuracy of reconstructions performed with this toolbox is always limited by the accuracy of the normalization applied. Therefore, special attention has to be paid to the normalization results prior to using the reconstruction algorithms of the toolbox. Besides the original approach of (Schönecker et al., 2009), a modification of the same approach that also incorporates pre-operative MR-data, as well as a nonlinear approach based on the segmentation algorithm of SPM (e.g. see Witt et al., 2013) have been implemented in the toolbox. Furthermore, figures that depict the normalization step results in high resolution are also shown by the toolbox, allowing for good manual control of normalization accuracy.

On the other hand, a prominent advantage of processing in MNI space is the possibility of comparing electrode localizations within and across groups and even across centers. Group studies are hardly feasible when the imaging data is processed in native space. Even more importantly, a robust delineation of target regions such as the GPi or the ViM, is not un-demanding, since standard MR images of single subjects don't clearly mark their boundaries. Even the STN, which largely shows hypo-intense on T2-weighted MR images (Slavin et al., 2006), may not always be robustly evaluated solely based on a subject's post-operative MR volume, since the electrode artifacts may lead to subtle distortions which render the nucleus blurred or hidden under the artifact. In addition, when compared to histological atlases, MR imaging of the STN renders the nucleus smaller (Richter et al., 2004) and seems to favor the anterior half (Dormont et al., 2004). Therefore, atlases that are compiled from histological information (Jakab et al., 2012; Krauth et al., 2010; Morel, 2013; Yelnik et al., 2007) may represent the real anatomical target regions better than the subject's MR image. Atlases may even go beyond a structural definition of subcortical nuclei. As shown in Accolla et al. (2014), Castrioto et al. (2014), and Lambert et al. (2012), the STN can further be subdivided into functional zones that may be used best for post-surgical evaluation if they prevail in a standardized space.

The best solution would be to combine both approaches: subcortical segmentation routines could be used to extract patient-specific target regions based on preoperative MR-imaging. The segmented nuclei could then be normalized to MNI space together with the whole-brain MR-volumes (without a loss of accuracy), and both patient-specific nuclei and atlas data could be visualized. So far, however, most current subcortical segmentation algorithms do not or only partly support classical DBS target regions (Fischl et al., 2002; Patenaude et al., 2011).

Reconstructions using MR- or CT-imaging

The approach has been implemented to support both postoperative MR- and CT imaging since both techniques are variably used in DBS centers. In the majority of our DBS patients with a pulse generator implant

(Medtronic Kinetra or Activa PC), postoperative MR imaging has been obtained in a setting that uses send-and-receive coils in a 1.5 T horizontal bore MRI. Additionally, SAR-levels must be reduced to an amount of up to 0.1 W/kg body weight. Experience in many centers has demonstrated that higher field strengths may be applied safely (Larson et al., 2008; Lee et al., 2005; Marks et al., 2009; Pinsker et al., 2008b).

However, post-operative MR imaging is not standard in the clinical routines of all DBS centers (see e.g. Shin et al., 2007) and so, the toolbox is constructed to also allow for using postoperative CT scans. It has been argued that the artifact observed in MR-images does not exactly overlap with the hyper-dense regions in CT images (Lee et al., 2010), a fact that might also result from inaccuracies in image fusion which takes place on the coarse, full-brain level (Duffner et al., 2002). Our results suggest that the artifacts overlap precisely. However, this could only be evaluated in a limited number of patients. Phantom studies have shown that the artifact observed in MR-images has a correct localization (Pollo et al., 2004; Yelnik et al., 2003), and yet artifacts on MR-images displaying inaccuracies on single slices of the volume cannot be ruled out (Lee et al., 2010; Pinsker et al., 2008a; Sauner et al., 2010). Such single-slice inaccuracies need to be considered when using MR imaging to manually localize DBS-electrodes, but should not largely affect the results of the approach presented here, since this method fits a model to many slices of two MR acquisitions instead of single-slice data.

Calculation of volume of activated tissue (VAT)

The toolbox comprises two additional functions that i) let the user choose which of the electrodes are stimulated monopolarly and ii) calculate a VAT based on the actual stimulation parameters of the patient following the approach of (Mädler and Coenen, 2012). The model described by Mädler and colleagues is a quite simple model that has proven to estimate robust results of the VAT and takes only the parameter voltage gain and impedance into consideration. More advanced models use neural network modeling techniques (Chaturvedi et al., 2013) or take patient-specific diffusion based MR data (Butson and McIntyre, 2008) into account to model the VAT more accurately. We plan to further optimize and extend the functionality of the toolbox such that other models can be implemented, too.

Limitations

In this study, automatic electrode contact reconstructions were classified as "correct" if they were <2 mm away from the manual survey of the electrode placement. The purpose of this procedure was to evaluate the performance of the automatic trajectory and contact reconstruction algorithms. Moreover, it is important to note that the exact positioning of DBS electrodes within a patient's brain cannot be determined with absolute precision without histology. Factors that may influence "correctness" of the electrode model are, among others, distortion of MR imaging (Zaitsev et al., 2004), susceptibility artifacts from the DBS lead in post-operative MR (Schönecker et al., 2009) and accuracy of the normalization process, i.e. the co-registration to a subcortical atlas (Klein et al., 2009).

Thus, it is not feasible to estimate a confidence interval of accuracy of the procedure and imaging of DBS phantoms can measure only accuracies of parts of the processing steps (Pollo et al., 2004; Yelnik et al., 2003).

Further, some studies have shown that DBS electrode trajectories may get curved over time, especially due to post-operative pneumocephalus (Kim et al., 2010; van den Munckhof et al., 2010; note that a different study did not find significant displacement over time, Slotty et al., 2012). Thus, the trajectory, which is being modeled as a straight line in this approach may not accurately model the long-term results and has been used only as a processing step to asses DBS contact location.

Finally, imaging data for all patients were acquired in a single DBS center. However, the toolbox can be easily adjusted to allow reconstruction of

electrode placement when postoperative images have been acquired using different protocols.

Availability and outlook

The software project is made available to the scientific community in the form of a MATLAB® toolbox that may be used for scientific purposes (http://www.lead-dbs.org). Especially for the normalization steps, but also for some other processing steps, the toolbox uses SPM8 (www.fil.ion.ucl.ac.uk/spm/). To this date, the toolbox has been tested with quadripolar Medtronic electrodes that have been implanted either in STN, GPi or ViM. As an outlook, it should be mentioned that the toolbox has already been extended to support DBS-targeting in Cg25 or subcallosal cortex as applied in depression patients (Mayberg et al., 2005).

Conclusions

To the best of our knowledge, this toolbox is the first piece of freely available software that focuses on semi-automatic DBS electrode reconstructions based on postoperative MR- or CT-data and is able to visualize DBS lead trajectories and atlas data. It can be shown that the toolbox is useful to robustly localize DBS electrodes in a large and heterogeneous group of patients. Furthermore, the toolbox can be used to visualize DBS placement and to simulate stimulations by calculating the volume of activated tissue. In summary, these are powerful tools to analyze and better understand the effects of DBS surgery in clinical studies.

Acknowledgments

Conflict of interest

There are no conflicts of interest.

Appendix A. Supplementary data

Supplementary data to this article can be found online at http://dx.doi.org/10.1016/j.neuroimage.2014.12.002.

References

Accolla, E.A., Dukart, J., Helms, G., Weiskopf, N., Kherif, F., Lutti, A., Chowdhury, R., Hetzer, S., Haynes, J.-D., Kühn, A.A., Draganski, A.B., 2014. Brain tissue properties differentiate between motor and limbic basal ganglia circuits. Hum. Brain Mapp. 35 (10), 5083–5092.

Brown, P., Williams, D., 2005. Basal ganglia local field potential activity: character and functional significance in the human. Clin. Neurophysiol. 116, 2510–2519. http://dx.doi.org/10.1016/j.clinph.2005.05.009.

Brücke, C., Huebl, J., Schönecker, T., Neumann, W.-J., Yarrow, K., Kupsch, A., Blahak, C., Lütjens, G., Brown, P., Krauss, J.K., Schneider, G.-H., Kühn, A.A., 2012. Scaling of movement is related to pallidal γ oscillations in patients with dystonia. J. Neurosci. 32, 1008–1019.

Butson, C.R., McIntyre, C.C., 2008. Current steering to control the volume of tissue activated during deep brain stimulation. Brain Stimul. 1, 7–15.

Caire, F., Ranoux, D., Guehl, D., Burbaud, P., Cuny, E., 2013. A systematic review of studies on anatomical position of electrode contacts used for chronic subthalamic stimulation in Parkinson's disease. Acta Neurochir. (Wien) 155, 1647–1654. http://dx.doi.org/10.1007/s00701-013-1782-1 (discussion 1654).

Castrioto, A., Lhommée, E., Moro, E., Krack, P., 2014. Mood and behavioural effects of subthalamic stimulation in Parkinson's disease. Lancet Neurol. 13 (3), 287–305.

Cavanagh, J.F., Wiecki, T.V., Cohen, M.X., Figueroa, C.M., Samanta, J., Sherman, S.J., Frank, M.J., 2011. Subthalamic nucleus stimulation reverses mediofrontal influence over decision threshold. Nat. Neurosci. 14, 1462–1467.

Chaturvedi, A., Luján, J.L., McIntyre, C.C., 2013. Artificial neural network based characterization of the volume of tissue activated during deep brain stimulation. J. Neural Eng. 10, 056023.

Deuschl, G., Schade-Brittinger, C., Krack, P., Volkmann, J., Schäfer, H., Bötzel, K., Daniels, C., Deutschländer, A., Dillmann, U., Eisner, W., Gruber, D., Hamel, W., Herzog, J., Hilker, R., Klebe, S., Kloss, M., Koy, J., Krause, M., Kupsch, A., Lorenz, D., Lorenzl, S., Mehdorn, H.M., Moringlane, J.R., Oertel, W., Pinsker, M.O., Reichmann, H., Reuss, A., Schneider, G.-H., Schnitzler, A., Steude, U., Sturm, V., Timmermann, L., Tronnier, V., Trottenberg, T., Wojtecki, L., Wolf, E., Poewe, W., Voges, J., German Parkinson Study Group, Neurostimulation Section, 2006. A randomized trial of deep-brain stimulation for Parkinson's disease. N. Engl. J. Med. 355, 896–908.

Dormont, D., Ricciardi, K.G., Tandé, D., 2004. Is the subthalamic nucleus hypointense on T2-weighted images? A correlation study using MR imaging and stereotactic atlas data. AJNR Am. J. Neuroradiol. 25 (9), 1516–1523.

Duffner, F., Schiffbauer, H., Breit, S., Friese, S., Freudenstein, D., 2002. Relevance of image fusion for target point determination in functional neurosurgery. Acta Neurochir. (Wien) 144, 445–451. http://dx.doi.org/10.1007/s00701-002-0919-4.

Ellis, T.-M., Foote, K.D., Fernandez, H.H., Sudhyadhom, A., Rodriguez, R.L., Zeilman, P., Jacobson, C.E., Okun, M.S., 2008. Reoperation for suboptimal outcomes after deep brain stimulation surgery. Neurosurgery 63, 754–760 (discussion 760–1).

Fischl, B., Salat, D.H., Busa, E., Albert, M., Dieterich, M., 2002. Whole brain segmentation: automated labeling of neuroanatomical structures in the human brain. Neuron 33, 341–355.

Fonov, V., Evans, A.C., Botteron, K., Almli, C.R., McKinstry, R.C., Collins, D.L., Brain Development Cooperative Group, 2011. Unbiased average age-appropriate atlases for pediatric studies. NeuroImage 54, 313–327.

Frank, M.J., Samanta, J., Moustafa, A.A., Sherman, S.J., 2007. Hold your horses: impulsivity, deep brain stimulation, and medication in parkinsonism. Science 318, 1309–1312.

Frankemolle, A., Wu, J., Noecker, A.M., 2010. Reversing cognitive–motor impairments in Parkinson's disease patients using a computational modelling approach to deep brain stimulation programming. Brain 133 (Pt 3), 746–761.

Green, N., Bogacz, R., Huebl, J., Beyer, A.-K., Kühn, A.A., Heekeren, H.R., 2013. Reduction of influence of task difficulty on perceptual decision making by STN deep brain stimulation. Curr. Biol. 23, 1681–1684.

Hariz, G.M., Blomstedt, P., Koskinen, L.O.D., 2008. Long-term effect of deep brain stimulation for essential tremor on activities of daily living and health-related quality of life. Acta Neurol. Scand. 118, 387–394.

Jakab, A., Blanc, R., Berenyi, E., Szekely, G., 2012. Generation of individualized thalamus target maps by using statistical shape models and thalamocortical tractography. AJNR Am. J. Neuroradiol. 33, 2110–2116.

Keuken, M.C., Bazin, P.-L., Schäfer, A., Neumann, J., Turner, R., Forstmann, B.U., 2013. Ultra-high 7 T MRI of structural age-related changes of the subthalamic nucleus. J. Neurosci. 33, 4896–4900.

Keuken, M.C., Bazin, P.L., Crown, L., Hootsmans, J., Laufer, A., Müller-Axt, C., et al., 2014. Quantifying inter-individual anatomical variability in the subcortex using 7 T structural MRI. NeuroImage 94, 40–46. http://dx.doi.org/10.1016/j.neuroimage.2014.03.032.

Kim, Y.H., Kim, H.J., Kim, C., Kim, D.G., Jeon, B.S., Paek, S.H., 2010. Comparison of electrode location between immediate postoperative day and 6 months after bilateral subthalamic nucleus deep brain stimulation. Acta Neurochir. (Wien) 152, 2037–2045. http://dx.doi.org/10.1007/s00701-010-0771-x.

Klein, A., Andersson, J., Ardekani, B.A., Ashburner, J., Avants, B., Chiang, M.-C., Christensen, G.E., Collins, D.L., Gee, J., Hellier, P., Song, J.H., Jenkinson, M., Lepage, C., Rueckert, D., Thompson, P., Vercauteren, T., Woods, R.P., Mann, J.J., Parsey, R.V., 2009. Evaluation of 14 nonlinear deformation algorithms applied to human brain MRI registration. NeuroImage 46, 786–802. http://dx.doi.org/10.1016/j.neuroimage.2008.12.037.

Krack, P., Batir, A., Van Blercom, N., Chabardes, S., Fraix, V., Ardouin, C., Koudsie, A., Limousin, P.D., Benazzouz, A., LeBas, J.F., Benabid, A.-L., Pollak, P., 2003. Five-year follow-up of bilateral stimulation of the subthalamic nucleus in advanced Parkinson's disease. N. Engl. J. Med. 349, 1925–1934.

Krauth, A., Blanc, R., Poveda, A., Jeanmonod, D., Morel, A., Székely, G., 2010. A mean three-dimensional atlas of the human thalamus: generation from multiple histological data. NeuroImage 49, 2053–2062.

Kupsch, A., Benecke, R., Müller, J., Trottenberg, T., Schneider, G.-H., Poewe, W., Eisner, W., Wolters, A., Müller, J.-U., Deuschl, G., Pinsker, M.O., Skogseid, I.M., Roeste, G.K., Vollmer-Haase, J., Brentrup, A., Krause, M., Tronnier, V., Schnitzler, A., Voges, J., Nikkhah, G., Vesper, J., Naumann, M., Volkmann, J., Deep-Brain Stimulation for Dystonia Study Group, 2006. Pallidal deep-brain stimulation in primary generalized or segmental dystonia. N. Engl. J. Med. 355, 1978–1990.

Lambert, C., Zrinzo, L., Nagy, Z., Lutti, A., Hariz, M., Foltynie, T., Draganski, B., Ashburner, J., Frackowiak, R., 2012. Confirmation of functional zones within the human subthalamic nucleus: patterns of connectivity and sub-parcellation using diffusion weighted imaging. NeuroImage 60, 83–94.

Larson, P.S., Richardson, R.M., Starr, P.A., Martin, A.J., 2008. Magnetic resonance imaging of implanted deep brain stimulators: experience in a large series. Stereotact. Funct. Neurosurg. 86, 92–100.

Lee, M.W.Y., De Salles, A.A.F., Frighetto, L., Torres, R., Behnke, E., Bronstein, J.M., 2005. Deep brain stimulation in intraoperative MRI environment — comparison of imaging techniques and electrode fixation methods. Minim. Invasive Neurosurg. 48, 1–6.

Lee, J.Y., Kim, J.W., Lee, J.-Y., Lim, Y.H., Kim, C., Kim, D.G., Jeon, B.S., Paek, S.H., 2010. Is MRI a reliable tool to locate the electrode after deep brain stimulation surgery? Comparison study of CT and MRI for the localization of electrodes after DBS. Acta Neurochir. (Wien) 152, 2029–2036.

Lumsden, D.E., Ashmore, J., Charles-Edwards, G., Lin, J.-P., Ashkan, K., Selway, R., 2013. Accuracy of stimulating electrode placement in paediatric pallidal deep brain stimulation for primary and secondary dystonia. Acta Neurochir. (Wien) 155, 823–836.

Mädler, B., Coenen, V.A., 2012. Explaining clinical effects of deep brain stimulation through simplified target-specific modeling of the volume of activated tissue. AJNR Am. J. Neuroradiol. 33 (6), 1072–1080.

Marks, W.A., Honeycutt, J., Acosta, F., Reed, M., 2009. Deep brain stimulation for pediatric movement disorders. YSPEN 16, 90–98.

Mayberg, H.S., Lozano, A.M., Voon, V., McNeely, H.E., Seminowicz, D., Hamani, C., Schwalb, J.M., Kennedy, S.H., 2005. Deep brain stimulation for treatment-resistant depression. Neuron 45, 651–660.

Morel, A., 2013. Stereotactic Atlas of the Human Thalamus and Basal Ganglia. CRC Press.

Mueller, J., Skogseid, I.M., Benecke, R., Kupsch, A., Trottenberg, T., Poewe, W., Schneider, G.H., Eisner, W., Wolters, A., Müller, J.U., Deuschl, G., Pinsker, M.O., Roeste, G.K., Vollmer-Haase, J., Brentrup, A., Krause, M., Tronnier, V., Schnitzler, A., Voges, J., Nikkhah, G., Vesper, J., Naumann, M., Volkmann, J., Deep-brain Stimulation for Dystonia Study Group, 2008. Pallidal deep brain stimulation improves quality of life in segmental and generalized dystonia: results from a prospective, randomized sham-controlled trial. Mov. Disord. 23, 131–134.

Pallavaram, S., Yu, H., Spooner, J., D'Haese, P.-F., Bodenheimer, B., Konrad, P.E., Dawant, B.M., 2008. Intersurgeon variability in the selection of anterior and posterior commissures and its potential effects on target localization. Stereotact. Funct. Neurosurg. 86, 113–119.

Patenaude, B., Smith, S.M., Kennedy, D.N., Jenkinson, M., 2011. A Bayesian model of shape and appearance for subcortical brain segmentation. NeuroImage 56 (3), 907–922.

Pinsker, M.O., Herzog, J., Falk, D., Volkmann, J., Deuschl, G., Mehdorn, M., 2008a. Accuracy and distortion of deep brain stimulation electrodes on postoperative MRI and CT. Zentralbl. Neurochir. 69, 144–147.

Pinsker, M.O., Volkmann, J., Falk, D., Herzog, J., Alfke, K., Steigerwald, F., Deuschl, G., Mehdorn, M., 2008b. Electrode implantation for deep brain stimulation in dystonia: a fast spin-echo inversion-recovery sequence technique for direct stereotactic targeting of the GPI. Zentralbl. Neurochir. 69, 71–75.

Pollo, C., Villemure, J.G., Vingerhoets, F., Ghika, J., Maeder, P., Meuli, R., 2004. Magnetic resonance artifact induced by the electrode Activa 3389: an in vitro and in vivo study. Acta Neurochir. (Wien) 146, 161–164.

Prodoehl, J., Yu, H., Little, D.M., Abraham, I., Vaillancourt, D.E., 2008. Region of interest template for the human basal ganglia: comparing EPI and standardized space approaches. NeuroImage 39, 956–965.

Richter, E.O., Hoque, T., Halliday, W., Lozano, A.M., Saint-Cyr, J.A., 2004. Determining the position and size of the subthalamic nucleus based on magnetic resonance imaging results in patients with advanced Parkinson disease. J. Neurosurg. 100, 541–546.

Sarnthein, J., Péus, D., Baumann-Vogel, H., Baumann, C.R., Sürücü, O., 2013. Stimulation sites in the subthalamic nucleus projected onto a mean 3-D atlas of the thalamus and basal ganglia. Acta Neurochir. (Wien) 155, 1655–1660.

Sauner, D., Runge, M., Poggenborg, J., Maarouf, M., Sturm, V., Treuer, H., Hunsche, S., 2010. Multimodal localization of electrodes in deep brain stimulation: comparison of stereotactic CT and MRI with teleradiography. Stereotact. Funct. Neurosurg. 88, 253–258.

Schönecker, T., Kupsch, A., Kühn, A.A., Schneider, G.-H., Hoffmann, K.T., 2009. Automated optimization of subcortical cerebral MR imaging-atlas coregistration for improved postoperative electrode localization in deep brain stimulation. AJNR Am. J. Neuroradiol. 30, 1914–1921.

Schönecker, T., Gruber, D., Kivi, A., Müller, B., Lobsien, E., Schneider, G.-H., Kühn, A.A., Hoffmann, K.-T., Kupsch, A.R., 2014. Postoperative MRI localisation of electrodes and clinical efficacy of pallidal deep brain stimulation in cervical dystonia. J. Neurol. Neurosurg. Psychiatry. http://dx.doi.org/10.1136/jnnp-2014-308159 (Epub ahead of print).

Schupbach, W.M.M., 2005. Stimulation of the subthalamic nucleus in Parkinson's disease: a 5 year follow up. J. Neurol. Neurosurg. Psychiatry 76, 1640–1644.

Schuurman, P.R., Bosch, D.A., Bossuyt, P.M., Bonsel, G.J., van Someren, E.J., de Bie, R.M., Merkus, M.P., Speelman, J.D., 2000. A comparison of continuous thalamic stimulation and thalamotomy for suppression of severe tremor. N. Engl. J. Med. 342, 461–468.

Shin, M., Lefaucheur, J.P., Penholate, M.F., Brugières, P., Gurruchaga, J.M., Nguyen, J.P., 2007. Subthalamic nucleus stimulation in Parkinson's disease: postoperative CT–MRI fusion images confirm accuracy of electrode placement using intraoperative multi-unit recording. Neurophysiol. Clin. 37, 457–466.

Slavin, K.V., Thulborn, K.R., Wess, C., 2007. Direct visualization of the human subthalamic nucleus with 3 T MR imaging. AJNR Am. J. Neuroradiol. 27 (1), 80–84.

Slotty, P.J., Kamp, M.A., Wille, C., Kinfe, T.M., Steiger, H.J., Vesper, J., 2012. The impact of brain shift in deep brain stimulation surgery: observation and obviation. Acta Neurochir. (Wien) 154, 2063–2068. http://dx.doi.org/10.1007/s00701-012-1478-y (discussion 2068).

Starr, P.A., Vitek, J.L., DeLong, M., Bakay, R.A., 1999. Magnetic resonance imaging-based stereotactic localization of the globus pallidus and subthalamic nucleus. Neurosurgery 44, 303–313 (discussion 313–4).

Tisch, S., Zrinzo, L., Limousin, P., Bhatia, K.P., Quinn, N., Ashkan, K., Hariz, M., 2007. Effect of electrode contact location on clinical efficacy of pallidal deep brain stimulation in primary generalised dystonia. J. Neurol. Neurosurg. Psychiatry 78, 1314–1319.

Tzourio-Mazoyer, N., Landeau, B., Papathanassiou, D., Crivello, F., Etard, O., Delcroix, N., Mazoyer, B., Joliot, M., 2002. Automated anatomical labeling of activations in SPM using a macroscopic anatomical parcellation of the MNI MRI single-subject brain. NeuroImage 15, 273–289.

van den Munckhof, P., Contarino, M.F., Bour, L.J., Speelman, J.D., de Bie, R.M.A., Schuurman, P.R., 2010. Postoperative curving and upward displacement of deep brain stimulation electrodes caused by brain shift. Neurosurgery 67, 49–53. http://dx.doi.org/10.1227/01.NEU.0000370597.44524.6D (discussion 53–4).

Vidailhet, M., Vercueil, L., Houeto, J.-L., Krystkowiak, P., Benabid, A.-L., Cornu, P., Lagrange, C., Tézenas du Montcel, S., Dormont, D., Grand, S., Blond, S., Detante, O., Pillon, B., Ardouin, C., Agid, Y., Destée, A., Pollak, P., French Stimulation du Pallidum Interne dans la Dystonie (SPIDY) Study Group, 2005. Bilateral deep-brain stimulation of the globus pallidus in primary generalized dystonia. N. Engl. J. Med. 352, 459–467.

Volkmann, J., Wolters, A., Kupsch, A., Müller, J., Kühn, A.A., Schneider, G.-H., Poewe, W., Hering, S., Eisner, W., Müller, J.-U., Deuschl, G., Pinsker, M.O., Skogseid, I.-M., Roeste, G.K., Krause, M., Tronnier, V., Schnitzler, A., Voges, J., Nikkhah, G., Vesper, J., Classen, J., Naumann, M., Benecke, R., DBS study group for dystonia, 2012. Pallidal deep brain stimulation in patients with primary generalised or segmental dystonia: 5-year follow-up of a randomised trial. Lancet Neurol. 11, 1029–1038.

Welter, M.-L., Schüpbach, M., Czernecki, V., Karachi, C., Fernandez-Vidal, S., Golmard, J.-L., Serra, G., Navarro, S., Welaratne, A., Hartmann, A., Mesnage, V., Pineau, F., Cornu, P., Pidoux, B., Worbe, Y., Zikos, P., Grabli, D., Galanaud, D., Bonnet, A.-M., Belaid, H., Dormont, D., Vidailhet, M., Mallet, L., Houeto, J.-L., Bardinet, E., Yelnik, J., Agid, Y., 2014. Optimal target localization for subthalamic stimulation in patients with Parkinson disease. Neurology 82, 1352–1361.

Witt, K., Granert, O., Daniels, C., Volkmann, J., Falk, D., van Eimeren, T., Deuschl, G., 2013. Relation of lead trajectory and electrode position to neuropsychological outcomes of subthalamic neurostimulation in Parkinson's disease: results from a randomized trial. Brain 136, 2109–2119.

Wodarg, F., Herzog, J., Reese, R., Falk, D., Pinsker, M.O., Steigerwald, F., Jansen, O., Deuschl, G., Mehdorn, H.M., Volkmann, J., 2012. Stimulation site within the MRI-defined STN predicts postoperative motor outcome. Mov. Disord. 27, 874–879.

Wu, M., Sheu, L.K., Andreescu, C., Becker, J.T., Tanase, C., 2009. Template selection for fMRI studies of elderly subjects. Proc. Int. Soc. Magn. Reson. Med. https://www.academia.edu/2684337/Template_Selection_for_fMRI_Studies_of_Elderly_Subjects/ (abstract).

Yelnik, J., Damier, P., Demeret, S., Gervais, D., Bardinet, E., Bejjani, B.-P., François, C., Houeto, J.-L., Arnule, I., Dormont, D., Galanaud, D., Pidoux, B., Cornu, P., Agid, Y., 2003. Localization of stimulating electrodes in patients with Parkinson disease by using a three-dimensional atlas-magnetic resonance imaging coregistration method. J. Neurosurg. 99, 89–99.

Yelnik, J., Bardinet, E., Dormont, D., Malandain, G., Ourselin, S., Tandé, D., Karachi, C., Ayache, N., Cornu, P., Agid, Y., 2007. A three-dimensional, histological and deformable atlas of the human basal ganglia. I. Atlas construction based on immunohistochemical and MRI data. NeuroImage 34, 618–638.

Zaitsev, M., Hennig, J., Speck, O., 2004. Point spread function mapping with parallel imaging techniques and high acceleration factors: fast, robust, and flexible method for echo-planar imaging distortion correction. Magn. Reson. Med. 52, 1156–1166.

Zhu, X.L., Hamel, W., Schrader, B., Weinert, D., Hedderich, J., Herzog, J., Volkmann, J., Deuschl, G., Müller, D., Mehdorn, H.M., 2002. Magnetic resonance imaging-based morphometry and landmark correlation of basal ganglia nuclei. Acta Neurochir. (Wien) 144, 959–969 (discussion 968–9).